Powder Technology 294 (2016) 226–235

Contents lists available at ScienceDirect

Powder Technology

journal homepage: www.elsevier.com/locate/powtec

An investigation on the properties of injection-molded pure iron potentially for biodegradable stent application

P. Mariot [a,*], M.A. Leeflang [b], L. Schaeffer [a], J. Zhou [b]

[a] Laboratory of Mechanical Transformation (LdTM), Faculty of Engineering, Federal University of Rio Grande do Sul, Av. Bento Gonçalves 9500, P.O Box 15021, 91501-970 Porto Alegre, RS, Brazil
[b] Department of Biomechanical Engineering, Delft University of Technology, 2628 CD Delft, The Netherlands

ARTICLE INFO

Article history:
Received 20 October 2015
Received in revised form 16 February 2016
Accepted 20 February 2016
Available online 24 February 2016

Keywords:
Iron
Biodegradable material
Metal injection molding
In vitro degradation
Corrosion

ABSTRACT

Metal injection molding (MIM) is a near-net-shape manufacturing process suitable for the production of small-size and complex-shape components. As a cost-effective and flexible manufacturing method, it may have distinct advantages over other methods when it comes to the manufacturing of implantable medical devices. However, up till now, the potential for MIM to be employed in the commercial-scale manufacturing of implantable medical devices has been insufficiently exploited. In the present research, an attempt was made to produce porous pure iron, as a metallic degradable biomaterial potentially for stent application, via the MIM route. The effects of iron powder loading and sintering temperature on the porosity, microstructure, mechanical properties, surface properties and in vitro degradation behavior of MIM iron were investigated. The results obtained were compared to those of cast iron. It was found that the amount of porosity retained in the as-sintered specimens had a major effect on their surface and mechanical properties. MIM iron exhibited strengths between those of magnesium alloys and 316 L stainless steel and very high ductility — a specially required property of stent materials. Its degradation rates in Hank's solution were superior to the degradation rate of cast iron. Interestingly, the material made from the feedstock containing 66% of iron powder, above the critical powder loading, showed the highest elongation and a good in vitro degradation rate. In conclusion, MIM is a promising method to be developed as a new route to produce thin-wall tubes for biodegradable stents.

1. Introduction

In 1991, Mullins et al. [1] and O'Laughlin et al. [2] introduced the principle of angioplasty in combination with the implantation of a stent into stenotic and hypoplastic artery of the patient with a congenital heart defect. Since then, the use of stents, made of stainless steel 316 L, shape-memory alloy Nitinol or cobalt–chromium alloys and typically having an outside diameter of 2.5–4.0 mm, a length of 8–38 mm and a wall thickness of 0.1–0.2 mm [3], has become widespread in treating numerous vascular diseases [4]. The growing interest in stenting is mainly due to the unprecedented success in enlarging the vessel lumen, reducing restenosis rates, being able to cover dissections, and reducing early ischemic complications, as compared with angioplasty alone [5,6]. Although coronary stents have remarkably improved the treatment of vascular diseases, there are still some disadvantages of stent implantation, such as chronic inflammation, restenosis and late-stage thrombosis, partly because of the permanent residence of stents in the body [4,5]. Release of metal ions, i.e., the corrosion products at the implantation site, may cause histological changes of the local tissue either by direct toxicants or through local hypersensitivity reactions, since the elements in stents, such as nickel, cobalt and chromium as well as their compounds are the known allergens [7]. Drug-eluting stents have been designed to reduce restenosis rates of bare-metal stents through localized release of anti-proliferative drugs, such as sirolimus and paclitaxel. The risk of late-stage thrombosis associated with drug-eluting bare-metal stents [5] is now dealt with by developing new thromboxane inhibitors as well as sophisticated stent surface structures that allow the loading and controlled release of the drugs [6].

In recent ten years, the development of biodegradable cardiovascular implants based on bare-metal corrosion has been considered as an alternative solution to avoiding the disadvantages of permanent stents [8,9]. The concept has been applied to magnesium-based coronary and peripheral stents [10]. It has however been found that too high corrosion rates of magnesium-based alloys result in dissatisfaction of the clinical requirements of stents to provide structural support over a period of 6–12 months when arterial remodeling and healing take place [10–12]. In vivo implantation of magnesium-based stents (made of the AE21 alloy) in the coronary artery of pigs, for example, revealed that due to a high corrosion rate of the magnesium alloy the implanted stents lost their mechanical integrity between 35 and 56 days [13].

Abbreviations: (MRI), Magnetic Resonance Imaging; (SFE), Surface Free Energy.

* Corresponding author.
E-mail addresses: paulo.mariot@ufrgs.br (P. Mariot), m.a.leeflang@tudelft.nl (M.A. Leeflang), schaefer@ufrgs.br (L. Schaeffer), J.Zhou@tudelft.nl (J. Zhou).

http://dx.doi.org/10.1016/j.powtec.2016.02.042
0032-5910/

Iron is another biodegradable metal with mechanical properties similar to 316 L stainless steel. It is an essential co-factor for a multitude of enzymes involved in diverse physiological processes, such as oxygen binding, DNA synthesis and redox enzyme activity. As such, it presents itself as an interesting candidate material for biodegradable stent applications. In vivo tests of iron stents have shown that pure iron exhibits a degradation rate slower than that estimated from in vitro testing results and thus faster degradation is desired [9,10], which may be achieved by modifying the chemical composition of iron, controlling its microstructure (grain structure and phase constituents) or introducing micro porosity. Fe–Mn alloys with magnetic resonance imaging (MRI) compatibility have been developed [14]. Powder metallurgy (P/M) and rolling-sintering steps have been taken to achieve desired microstructure and mechanical properties. Indeed, the degradation rates of Fe–Mn alloys can be increased by more than two times in comparison with pure iron [15]. The control of the distribution of porosity in the materials throughout processing via the P/M route has been found to be of critical importance, as the mechanical properties of the materials are also influenced by the porosity. To understand the mechanical behavior of stents, thin-wall tubes were made from rectangular bars by using wire electro-discharge machining and turning, followed by laser cutting, annealing and descaling [16]. The multi-step processing involved in stent fabrication led to surface irregularities such as pores, high roughness and even cracks. It became obvious that the adoption of suitable stent fabrication technologies was of critical importance in achieving desired physical, mechanical and chemical properties of biodegradable stents.

Metal injection molding (MIM) is a well-established P/M technology and a viable alternative to machining and investment casting. It has distinct advantages in producing small, complex shapes in large quantities and has been applied in the manufacturing of components in cars, aerospace vehicles, medical instruments and telecommunication equipment. Micro MIM technology that has been intensively developed in recent years is capable of achieving thin walls down to 20 μm and surface roughness values less than 0.05 μm [17], which demonstrates the MIM technology readiness to produce thin-wall tubes as the precursors of stents. As a matter of fact, MIM has been successfully utilized to produce tubes with longitudinal and circumferential channels for drug-eluting stents [18]. Thin-wall stainless steel tubes with outside diameters of 1.524 to 2.413 mm and wall thicknesses of 0.05 to 0.25 mm were realized as an embodiment of the MIM technology developed and patented [18]. Clearly, from a geometrical point of view, the MIM technology is able to satisfy the requirements of thin-wall tubes for stents. However, no research has ever been performed on the MIM process for biodegradable iron stent precursors. From a microstructural point of view, the MIM technology is of great interest, because it offers a porous microstructure, allowing accelerated degradation of iron in physiological environments and providing drug reservoir capabilities. The key lies in the control of micro porosity to reach an optimum balance between degradation rate and mechanical properties. Micro pores on the surface affect surface roughness and in turn have a direct impact on cellular responses [4]. Many studies have in recent years been conducted to determine the influence of surface chemistry and topography on cellular responses [6].

The present study was the first attempt to develop the MIM technology for pure iron as a biodegradable metal potentially for stents. Particular attention was paid to the interplay between MIM material and process parameters (i.e., powder loading in MIM feedstock and sintering temperature), porosity, mechanical properties, surface roughness, surface energy and degradation behavior of MIM iron. The main objective was to assess the potential of applying the MIM technology to produce iron products for biodegradable stents in the near future.

2. Materials and methods

2.1. MIM feedstock and specimen preparation

In this research, an iron powder with a carbon concentration of 0.02%, spherical particle shape and a median particle size of 3.61 μm was used to prepare MIM feedstock. A multi-component binder system consisting of paraffin wax, polypropylene and stearic acid was employed in feedstock preparation. The volumetric compositions of the feedstock are given in Table 1. The powder and binder were blended in a glove box under a protective atmosphere with oxygen content <0.5 ppm to minimize oxidation. The feedstock was prepared at 175 °C with the binder melted first and then the iron powder added incrementally. Powder loadings in the feedstock were 54, 58, 62 and 66%. These iron powder loadings were chosen based on the value (56%) used in earlier research on MIM of pure iron [19] and on the consideration of a range around the critical iron powder loading (63% by volume) so as to illustrate the effect of powder loading in the present MIM feedstock — a material variable on the resultant porosity, mechanical properties and degradable behavior of the materials after sintering.

The critical powder loading was determined in accordance with the method described in [20]. A Haake Rheomix 3000p rheometer with blade-type rotors coupled with a Haake Rheocord 252p module was used. At a temperature of 175 °C and a rotor speed of 40 rpm, torque changes with time were monitored. The iron powder was added at a step of 1 vol% from 60% in the feedstock. The experiment was stopped when the mixing torque increased significantly and became erratic, indicating the attainment of the critical loading. The effect of iron powder loading on the mixing torque is shown in Fig. 1.

The feedstock was afterwards pelletized. Injection molding was performed by using a 12.5 MPa injection molding machine to produce dog-bone-shaped tensile specimens with a nominal length of 95 mm and a square gauge area of 15.6 mm^2. Debinding was realized in a two-step solvent/thermal operation. Green parts were solvent debound in heptane at 60 °C for 4 h, followed by thermal debinding during heating at a slow rate. Weight losses during solvent debinding are given in Table 2. Sintering of all specimens was performed in a furnace with a reducing atmosphere composed of H_2 and Ar. The sintering cycle was as follows: heating at a rate of 0.5 °C/min to 450 °C for thermal debinding and pre-sintering. This heating hate was considerably lower than the values found in the literature for the thermal debinding of titanium [21,22] and 316 L stainless steel [23] in order to minimize the retention of the binder in sintered specimens. A heating rate of 5 °C/min to the sintering temperature was employed, followed by cooling to room temperature at 10 °C/min in a hydrogen atmosphere. Three different sintering temperatures, i.e., 1040, 1080 and 1120 °C in the typical range for the sintering of iron, were used to reach different porosity levels.

As the process involves the use of the binder and the debinding step, concerns may be raised about the remaining binder in the sintered product. The biocompatibility of MIM samples was determined and the results were reported in the literature for stainless steel (316 L) [5] and titanium [21,22]. The biocompatibility of porosity-free pure iron was also investigated [9,24–26]. Furthermore, in vivo tests were performed in the case of pure iron and no particular toxicity issues were raised.

Table 1
Volumetric compositions of the feedstock for MIM.

Component	Volume (%)			
Pure iron	54	58	62	66
Polypropylene	19.7	18.7	17.7	16.9
Paraffin wax	19.3	18.5	18.0	17.5
Stearic acid	3.0	2.8	2.3	1.9

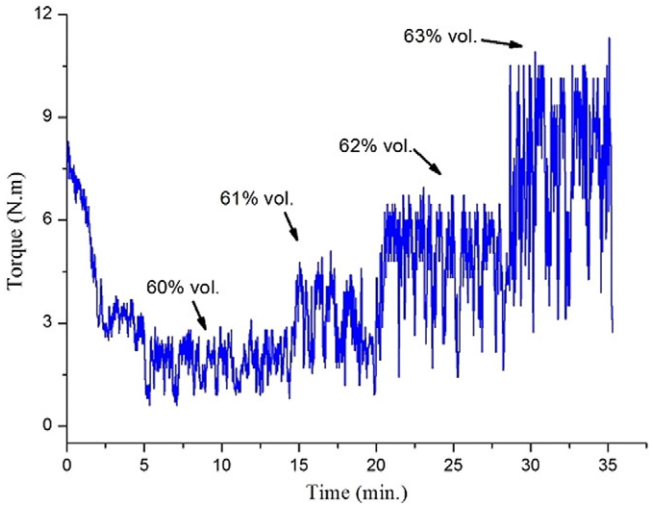

Fig. 1. Mixing torque as a function of time for 60, 61, 62 and 63 vol% iron powder loading.

2.2. Physical and mechanical tests

2.2.1. Porosity

Sintered density was determined by using the immersion method (Archimedes' principle), according to ASTM B311 [27]. This method was previously used for the measurement of the densities of biomaterial specimens with porosity levels between 4 [28] and 28% [29]. Five samples prepared under the same processing conditions were used to ensure the reliability of the results.

2.2.2. Microstructure

For metallographic examination, samples were cut from tensile bars into square blocks with sizes of 0.8 × 4 × 4 mm, ground and polished to a 0.3 μm surface finish. The polished samples were etched with dilute nitric acid (3%) for optical metallography and characterized by using an optical microscope (Leica DFC-320).

2.2.3. Surface roughness

The surface roughness of sintered samples was determined using a Taylor–Hobson Surtronic 3 + surface roughness meter. The average surface roughness, R_a, is defined as the arithmetic mean of the deviations of protrusions and depressions from the average line shown on the roughness profile. Three samples from each group were measured three times. The results are presented as mean values ± standard deviations (SD).

2.2.4. Surface free energy

Dynamic advancing contact angles were determined using a Krüss DSA 100 drop shape analyzer with deionized water and diiodomethane as wetting liquids. 10 μl wetting liquid was placed on the testing surface by means of a syringe. Upon contact with the surface, the increasing droplet profile was measured at an interval of 1 s for 33 s. For every sample, triplicate measurements were performed with each of the two different wetting liquids. Surface free energy (SFE) was calculated by applying Fowkes' theory. The values reported in this paper represent the average and standard deviations (SD) for contact angles in water, total surface free energy, dispersive and polar components of the total surface free energy.

Table 2
Weight losses of specimens with different iron powder loadings during solvent debinding.

Iron powder loading (%)	Weight loss (%)	Standard deviation
54	2.61	0.17
58	2.47	0.22
62	1.83	0.08
66	2.21	0.19

2.2.5. Tensile tests

Tensile tests were performed using a Zwick Z-100 mechanical tester at a crosshead speed of 1 mm/min. Five samples for each condition were used to ensure the reliability of the results.

2.3. Immersion tests

Dynamic immersion tests were performed in flowing Hank's solution according to ASTM-G31-72 [30]. Samples were immersed in the solution at 37 °C for 5, 10, 15 and 20 days. Then, the samples were taken out of Hank's solution, gently rinsed with distilled water and alcohol, and dried at room temperature. These samples were cleaned using a solution composed of 595 g/l hydrochloric acid and 3.5 g/l hexamethylene tetramine to remove surface corrosion products, rinsed with alcohol, dried at room temperature and finally weighed to calculate the weight loss and weight loss rate: weight loss = (weight before immersion − weight after cleaning) / surface area; weight loss rate = (weight before immersion − weight after cleaning) / (surface area × immersion time). The weights of the sample before and after immersion were measured by using a balance with an accuracy of 0.1 mg. The morphologies and microstructures of immersed samples were characterized by using a scanning electron microscope (JEOL, JSM6335F).

3. Results and discussion

3.1. Critical powder loading in MIM feedstock

Fig. 1 shows the mixing torque as a function of mixing time at various iron powder loadings. At each point where iron powder was added to the mixture, the mixing torque showed a jump and then settled to a near-steady-state value associated with the homogenization of the mixture. As described in the previous research [20], once the critical powder loading is exceeded, excessive powder loading makes the mixture unstable. In the present investigation, 63 vol% appeared to be the critical powder loading, as it resulted in the highest magnitude of torque changes.

3.2. Weight loss at the solvent debinding

Weight losses during solvent debinding are given in Table 2. With a decrease in binder volume fraction, weight loss decreases, except for the specimens containing 66% iron powder in the feedstock, which suggested less retention of the binder after solvent debinding.

3.3. Porosity

Fig. 2 shows the relative sintered density (%) as affected by powder loading in the MIM feedstock. In this figure, the sintering temperature used was 1080 °C. It was observed that an increase in iron powder loading led to an increase in the densification of samples up to 62% powder loading. Furthermore, samples showed decreases in shrinkage with increasing iron powder loading up to 62%, corresponding to the increases in densification.

The sintered density of the sample initially containing 62% iron powder in the feedstock was about 95% of the theoretical density, which was the highest densification achieved among all the samples. As a porosity level of 8% represents a critical value, below which most of pores become closed ones, it is reasonable to believe that in this sample the majority of pores became closed ones, while the other samples with other initial powder loadings had more open pores than closed ones. The high densification of the sample with 62% powder loading in the feedstock was due to the powder loading that was close to the critical powder

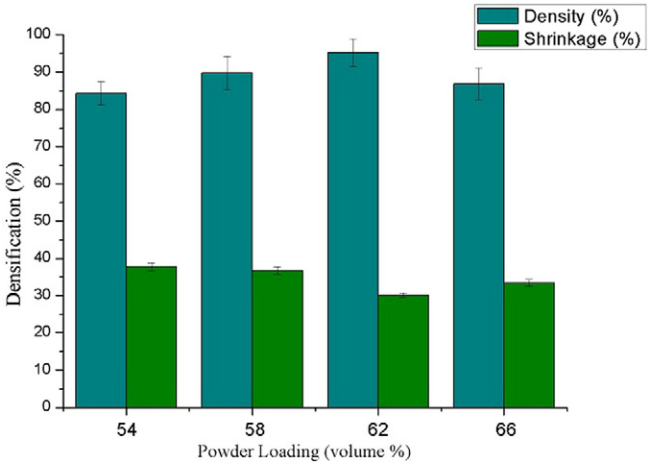

Fig. 2. Densification and shrinkage as a function of pure iron powder loading.

loading (63 vol%). With a further increase in powder loading to 66%, densification became less than that of the sample with 62% powder loading. Obviously, this result is related to the critical powder loading of the feedstock used in this work and also the sintering temperature. These two influencing factors will be discussed in next section on the porous microstructures of sintered samples.

3.4. Microstructure

Fig. 3 shows the porous structures of iron samples prepared from the feedstocks with iron powder loadings ranging from 54 to 66 vol% and sintered at 1080 °C, in order to depict the effect of powder loading in the feedstock clearly. For comparison purposes, Fig. 3e shows the microstructure of cast pure iron that contained well-distributed fine pores. While the sample (Fig. 3a) initially containing 54% iron powder in the MIM feedstock showed an irregular distribution of pore sizes and a large amount of porosity, the sample initially containing 66% iron powder (Fig. 3d) showed a larger average pore size, a more regular distribution of pore sizes and larger pore interspace. The other two MIM samples showed intermediate microstructures. The sample initially

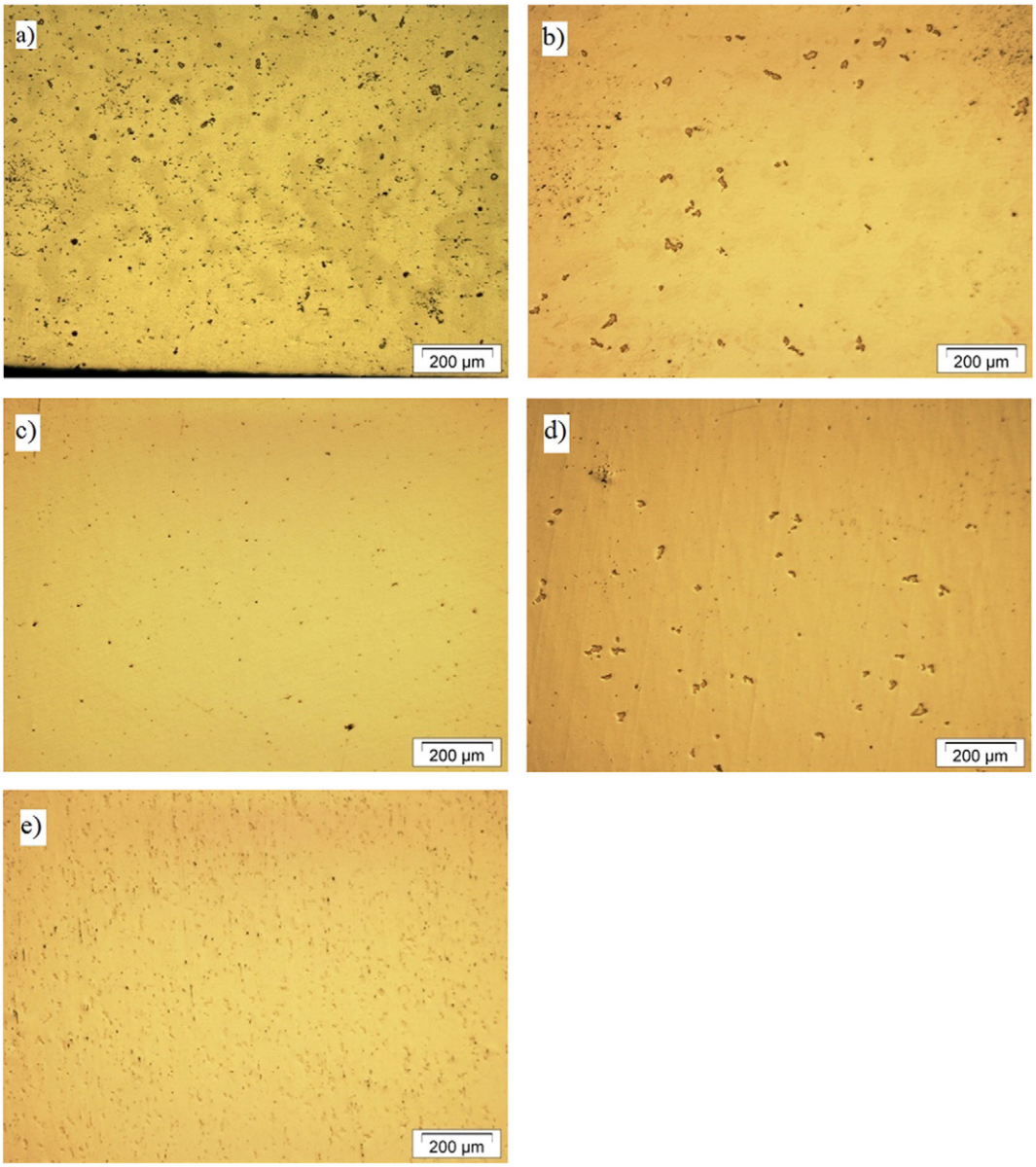

Fig. 3. Sintered pure iron with (a) 54, (b) 58, (c) 62, (d) 66% powder loading, sintered at 1080 °C and (e) cast pure iron.

containing 62% iron powder in the feedstock (Fig. 3c) showed the smallest pore sizes and large pore interspace, thus confirming the densification values reported earlier (Fig. 2). This structure was achieved due to the powder loading that was close to the critical powder loading (63% by volume). While the sample initially containing 62% powder had smaller pores, the sample initially with 66% powder had coalesced, larger pores and greater pore interspace. Such microstructural features were also found by Chen et al. [31] in biomedical titanium alloys.

The porosity of the sample with 54% iron powder loading was higher than that of the sample initially containing 66% iron powder. As pores in the sintered material could act as stress concentrators, it was expected that the mechanical properties of the sample with a higher level of porosity would be lower [31,32]. Exceeding the critical powder loading (63% by volume) led to a less regular pore distribution and increased pore sizes, when compared with the sample with a powder loading near the critical value (Fig. 3c). Li et al. [32] reported that when powder loading was higher than the critical one, there would be no sufficient binder to fill into the space between powder particles. As a result, there could be voids formed in the feedstock. This could explain the coalesced pore structure shown in Fig. 3d. The observation of porosity in the microstructures is in agreement with the densification results shown in Fig. 2.

Fig. 4 shows the microstructures of the samples prepared from the feedstock with an iron powder loading of 54% and sintered at 1040, 1080 and 1120 °C (Fig. 4a, b and c, respectively). These samples initially having a low iron powder loading were selected due to the relatively high levels of porosity to allow the effect of sintering temperature on the porous structure of MIN iron to be clearly indicated. As can be seen, an increase in sintering temperature led to decreases in pore number density and pore sizes. The sintering temperature also influenced the pore size distribution. While the sample sintered at 1040 °C showed an irregular distribution of pore sizes, the samples sintered at 1080 and 1120 °C showed a large number of small pores as well as relatively large pores and smaller pore interspace. This influence is similar to that of powder loading (Fig. 3) and well documented in P/M and MIM technologies. As found in the case of sintering injection-molded niobium [33] and pure iron [34], an increase in sintering temperature led to increases in sintered density and shrinkage as a result of improved boundary diffusion and volume diffusion, which promoted the closure of pores. This influence was also reported by Čapek and Vojtěch [35] in the case of sintering magnesium. In the case of sintering injection-molded niobium in vacuum, a higher sintering temperature was found to facilitate the removal of oxygen from the as-received powder, thereby contributing to densification [33].

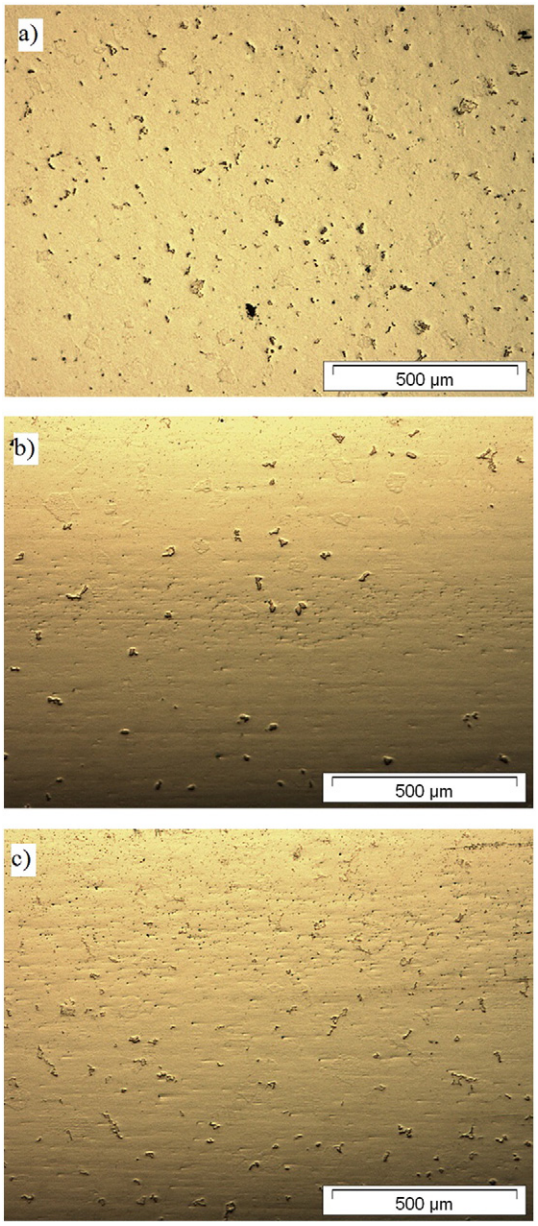

Fig. 4. Sintered pure iron with 54% powder loading, sintered at (a) 1040, (b) 1080 and (c) 1120 °C.

3.5. Mechanical properties

Fig. 5 shows the stress–strain curves of sintered pure iron samples with different initial powder loadings, sintered at 1120 °C (Fig. 5a) and those of the samples with an initial powder loading of 66% and sintered at different temperatures (Fig. 5b). The data are given in Table 3. In general, an increase in powder loading, as expected, led to an increase in ultimate tensile strength. With decreasing powder loading, elongation at fracture markedly reduces.

The observed mechanical behaviors of the samples were quite consistent with the porous structure variation shown in Fig. 3a, b and c. Pore volume decreased with increasing powder loading between 54 and 62% and then increased. As porosity had a direct influence on the mechanical strength, the yield strength increased from 59 MPa (54 vol%) to 87 MPa (62 vol%) and the ultimate tensile strength of the sample with 62% powder loading reached the highest value, because the resistance to deformation increased with decreasing porosity. A further increase in powder loading to 66% resulted in a small decline in ultimate tensile strength from 210 MPa (Fig. 5a), indicating that porosity was indeed a predominant factor deciding the tensile strength of porous pure iron.

The plateau in the stress–strain curves between 15 and 40% elongation, shown by the samples initially containing 62 and 66% iron powder in the MIM feedstock, could be associated to the events of cyclic buckling, flow and fracture of pore walls, as reported earlier on the fracture of sintered Fe–30%Ni alloys [36]. Comparing the mechanical behaviors of these two samples, the 66% sample showed a greater elongation at fracture (50%) than the sample initially containing 62% iron powder (40.8%). It suggested that a lower pore number density shown by the 66% iron sample corresponded to a higher ductility, when compared with the finer and regularly distributed pore structure shown by the 62% iron sample. The behavior of the 66% sample could be explained by less crack initiation sites and longer crack propagation paths during tensile testing (Fig. 3d). A large ductility is a particularly welcome property of a material for coronary stents, because stents are subjected to extensive plastic deformation during implantation (up to 20% in the most critical parts) [37].

Fig. 5b shows the mechanical behaviors of the samples initially containing 66% iron powder and sintered at different temperatures. Clearly,

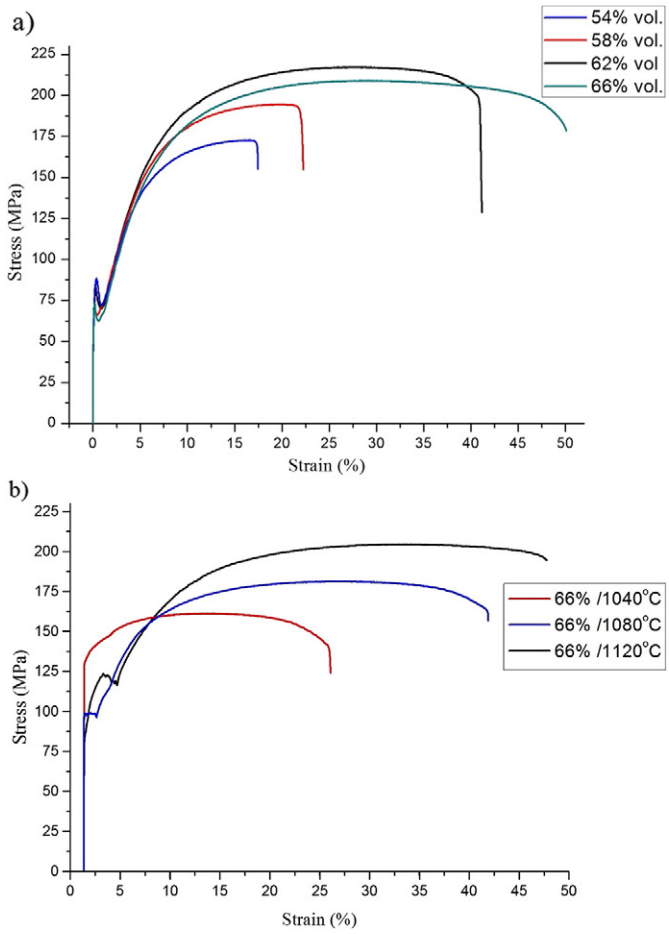

Fig. 5. Tensile stress–strain curves of the samples (a) with different initial iron powder loadings and sintered at 1120 °C and (b) with an initial powder loading of 66% and sintered at different temperatures.

an increase in sintering temperature led to an increase in ultimate tensile strength. This can be explained by the densification of the samples. As previously reported [33,34], with increasing sintering temperature, both boundary diffusion and volume diffusion were increased. As result, densification was enhanced, as shown in Fig. 4. An increase in densification led to an increase in ultimate tensile strength.

The maximum elongation was also increased from 26.4 to 50% as the sintering temperature increased from 1040 to 1120 °C (Fig. 5b). This can be explained by the decreases in the number density and sizes of pores in the 1120 °C sample and thus less crack initiation sites and longer crack propagation paths.

The appearance of the upper and lower yield points in the stress–strain curves (Fig. 5b) is likely associated with the formation of Lüders

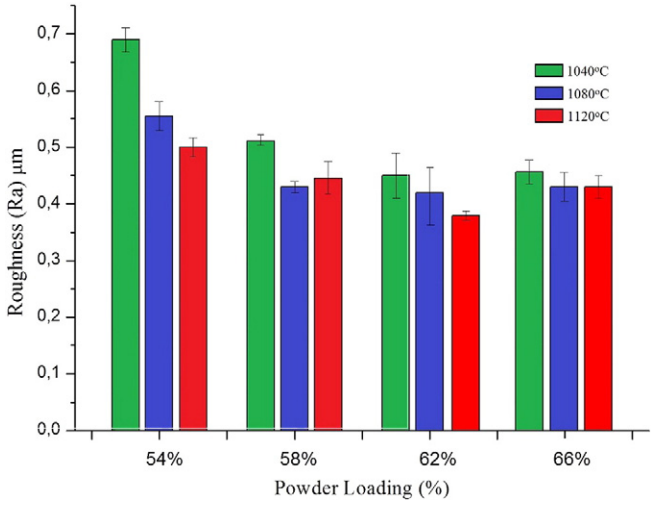

Fig. 6. Roughness Ra values of the samples initially with 54, 58, 62 and 66% iron powder loadings and sintered at three different temperatures.

bands, as explained by Song et al. [38]. The authors reported that in pure iron manufactured by using the selective laser melting method, this phenomenon is characterized by the formation of specific areas of plastic deformation, causing local mechanical strengthening, followed by necking, as a cyclic event.

Young's moduli of the sintered specimens determined from the tensile tests were 90, 105, 178 and 110 GPa for the (54%/1040 °C), (58%/1120 °C), (62%/1120 °C) and (66%/1120 °C) samples, respectively. In general, at a higher sintering temperature, pore number density decreased and thus a larger amount of energy was necessary for elastic deformation. As a comparison, Song et al. [38] reported a Young's modulus of 205 GPa for cast pure iron and 190 GPa for 316 L stainless steel. Banerjee [39] reported a Young's modulus of 110 GPa for titanium and Bowen [40] reported a Young's modulus of 44 GPa and an elongation value of 13% for a biodegradable magnesium alloy potentially for stent application. The comparison shows that the MIM pure iron investigated in this work had mechanical properties between those of magnesium alloys and 316 stainless steel and superior ductility, all of which are the suitable mechanical properties of a biodegradable material for stent application. Comparing the mechanical properties of the samples tested in this work, the best choice in terms of the mechanical behavior is the sample initially containing 66% iron powder, because it has a high mechanical strength and elongation, both of which are needed for the delivery, expansion and functioning of the stent.

3.6. Surface roughness

Fig. 6 shows the roughness values of MIM samples, affected by powder loading in the feedstock and sintering temperature. The sample

Table 3
Tensile properties of MIM iron as affected by iron powder loading and sintering temperature.

Condition	Yield strength (MPa)	Young's modulus (GPa)	Elongation (%)	Standard deviation
54%/1040 °C	59	90	13	5.5
54%/1080 °C	–	–	–	–
54%/1120 °C	86	101	17.3	2.6
58%/1040 °C	73	95	10	4.8
58%/1080 °C	84	100	24.5	2.6
58%/1120 °C	85	105	22.2	1.5
62%/1040 °C	96	91	12	4.9
62%/1080 °C	139	165	16	3.8
62%/1120 °C	87	178	40.8	4.0
66%/1040 °C	128	110	26.4	5.4
66%/1080 °C	100	128	42.5	4.3
66%/1120 °C	114	110	50	3.2

with a higher volume fraction of pores (54%/1040 °C) corresponded to a higher surface roughness, whereas there were no significant differences in surface roughness between the samples with 58, 62 and 66% powder loadings.

For the samples initially containing 54% iron powder, an increase in sintering temperature led to a decrease in roughness. The mean surface roughness value presented by the sample 54%/1040 °C (~0.7 *Ra*) was quite close to that mentioned by Demangel et al. [21] who studied the properties of titanium as a biomaterial for implants and considered this value ideal for endothelialization. Considering the fact that for the application of a biodegradable stent material fibroblast proliferation above a certain value is undesired, one may choose a roughness value, e.g., 0.4 R_a that was achieved for the sample with a powder loading of 62% and sintered at 1120 °C.

3.7. Surface energy

Contact angles and surface energy values calculated from contact angles are shown in Fig. 7. The last two bars in each figure compare the values between the sintering temperatures of 1040 and 1120 °C. As can be seen, a higher level of porosity corresponds to a higher surface energy. The figure also shows that an increase in sintering temperature results in a decrease in surface free energy. Basically, it is the surface free energy that determines the contact angle. Decreasing specific area by decreasing pore volume at the surface decreases surface free energy. Pore volume at the surface is therefore a determining factor for a change in surface free energy, while the sintering temperature has a minor effect on this variation. The effect of pore volume on the surface free energy is evident, when the samples containing 62% and 66% iron powder in the feedstock are compared. In this case, increasing the average pore diameter causes an increase in surface free energy.

It was reported by Huang [41] and Huan [42] that surface free energy was a major factor influencing the proliferation of fibroblasts and determining the degree of cell adhesion to the wall of the implant, which could be related to the occurrence of restenosis. Our results are in disagreement with the results obtained by Huang et al. who reported that for titanium specimens free of porosity the roughest surface had the highest water contact angle. From the results shown above (Fig. 7), it can be stated that porosity has a major influence on surface free energy. The values of surface free energy and contact angle show that the sample with 62% powder loading in the feedstock may exhibit the best behavior when employed as a material for biodegradable stents because of its relative low wettability.

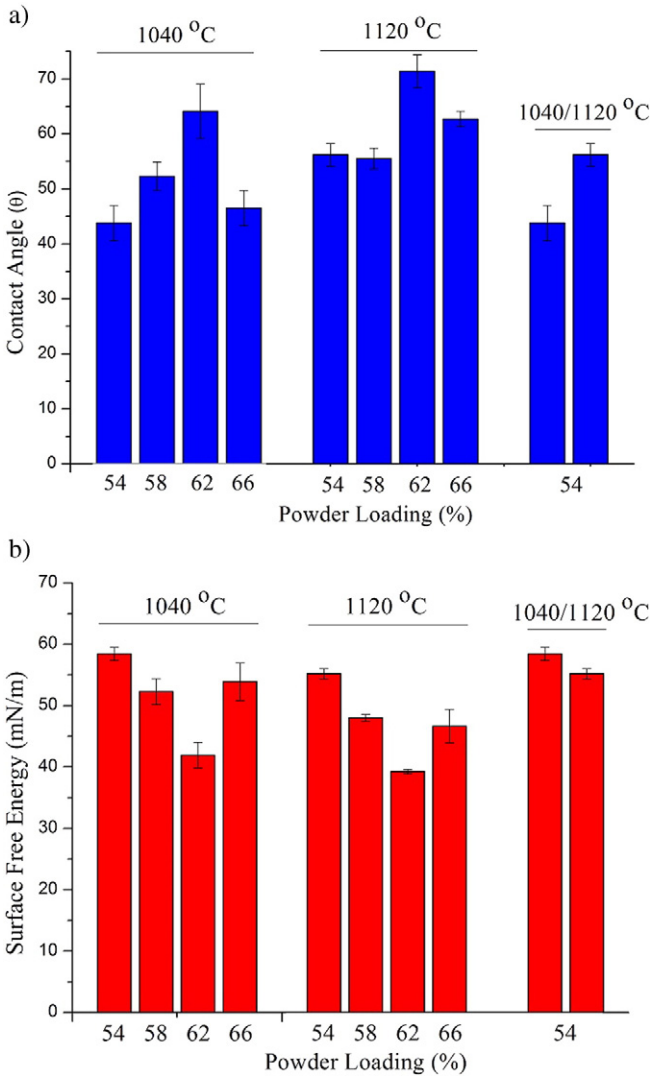

Fig. 7. Effects of powder loading and sintering temperature on (a) contact angle and (b) surface free energy.

3.8. In vitro degradation

Fig. 8 shows the results of immersion tests to evaluate the degradation behaviors of the samples. The degradation behavior was expected to be influenced by the porosity, especially the surface porosity and in turn by iron powder loading in the MIM feedstock and sintering temperature. From the weight loss measurements of the degraded samples between day 10 and day 20, it can be seen that the 58%/1080 °C sample had the highest degradation rate (0.047 g/A_0), followed by the 66%/1120 °C sample (0.042 g/A_0) and the 54%/1040 °C sample (0.040 g/A_0), although the differences between these sample groups were not really marked. A higher weight loss may be attributed to a higher level of porosity present in the sample, which can be compared between Fig. 3a, b and c.

The 62%/1120 °C sample exhibited the lowest degradation rate (0.0228 g/A_0), which was significantly lower than that of cast iron sample. This result is in agreement with the effect of porosity in MIM materials on corrosion, as reported before [21]. From the results of the samples with 54 and 58% powder loadings, after 20 days of immersion, it was observed that the increases in sintering temperature resulted in lower mass losses. This is because a higher sintering temperature leads to a lower level of porosity and smaller pore sizes, which decreases the specific surface area of the sample and results in a lower degradation rate.

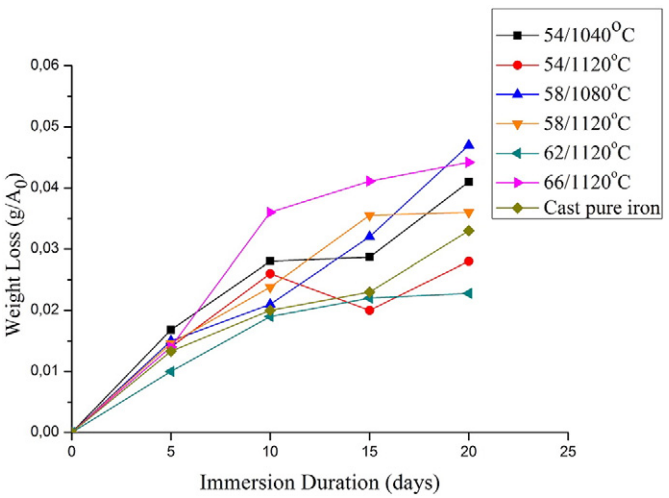

Fig. 8. Weight losses between day 0 and day 20 during immersion in Hank's solution.

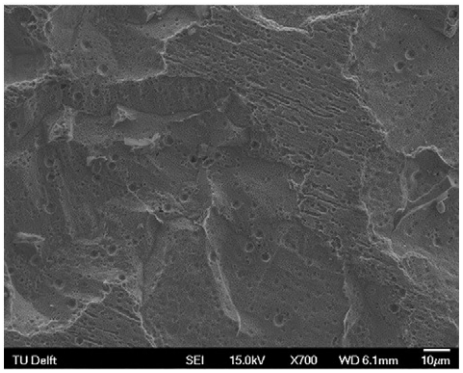

Fig. 9. Corroded surface of 62%/1120 °C sintered sample.

Up to 5 days of immersion, no significant differences in degradation rate were found between the samples, except the 54%/1040 °C and 62%/1120 °C samples with the highest and lowest porosity levels, respectively. After 10 days of immersion, no significant differences in degradation rate could be found between cast, 58%/1080 °C and 62%/1120 °C samples either. However, a considerable increase in degradation rate was observed for the 66%/1120 °C sample up to 10 days of immersion. Although this sample showed the largest pore interspace, it was also found that large pore sizes in this sample resulted in fast degradation. It was also found that for the 62%/1120 °C, cast and 66%/1120 °C samples there was a tendency of decreasing degradation rate after 10 days of immersion. The same behavior was observed for the 58%/1120 °C sample after 15 days. It might be explained by the formation of degradation products, i.e., an iron phosphate layer on the surface that could inhibit further degradation by hindering oxygen diffusion. A similar mechanism was described before [24,43] to explain the corrosion behavior of iron wires fabricated by casting and drawing. These studies showed that Fe_3O_4 with a low solubility, formed at the early stage of the corrosion process due to insufficient oxygen supply to the deposited $Fe(OH)_2$, resided at the innermost degradation layer in contact with the iron substrate and impeded further degradation of iron. Similarly, the FeP layer that had a low solubility in water impeded the degradation by hindering oxygen transport onto the iron surface.

In a neutral aqueous environment, iron degrades via the following reactions:

$$Fe_{(s)} \rightarrow Fe^{2+}_{(aq)} + 2\,\bar{e} \quad (1)$$

$$0_{2(g)} + 2H_2O_{(l)} + 4\,\bar{e} \rightarrow 4OH^-_{(aq)} \quad (2)$$

$$Fe^{2+}_{(aq)} + 2OH^-_{(aq)} \rightarrow Fe(OH)_{2\,(s)} \quad (3)$$

Inadequate supply of oxygen due to the deposited $Fe(OH)_2$ triggers the formation of Fe_3O_4 on the iron surface and slows oxygen diffusion onto the iron surface. Further corrosion is thus inhibited, as reported on the corrosion behavior of pure iron [24] and magnesium alloys [44,45]. After 20 days of immersion, cast pure iron showed a higher degradation rate when compared to the 54%/1120 °C sample. This behavior is explained by a large number of pores present in cast pure iron (Fig. 3e).

From the results shown in Fig. 8, it can be seen that MIM porous pure iron exhibits a degradation rate between the degradation rates of magnesium alloys [44,45] and cast pure iron [24]. This result suggests that MIM porous iron may indeed be an interesting candidate material for biodegradable coronary stents.

3.9. Corrosion mechanisms

Fig. 9 shows the morphology of the corroded 62%/1120 °C sample. The surface appears to have received a uniform attack by the immersion solution and no evidence of severe pitting corrosion could be found. This behavior can be related to the high density of the 62%/1120 °C sample.

Fig. 10 shows the morphology of the sample with 54% powder loading and sintered at 1040 °C. It can be seen that pitting is a predominant mechanism of corrosion. Pitting corrosion is usually related to the formation of a heterogeneous hydroxide layer that covers the surface. Cl^- ions from the solution can penetrate into the hydroxide layer to compensate for the increases of metal ions beneath the hydroxide layer. The hydrolysis by water or metal chlorides formed leads to the formation of hydroxide and free acid (Reaction 2), lowering the pH value at the spot area, while the bulk solution remains neutral [43]. This reaction leads to the formation of pits, as shown in detail in Fig. 10b. This behavior was reported before in the case of pore-free iron [24,25]. For a biodegradable stent, pitting corrosion could lead to its premature failure and therefore only the MIM material with a right powder loading and sintered under right conditions should be employed for biodegradable stents.

4. Conclusions

Sintered porous pure iron with relative density values between 84 and 95% of the theoretical value, aimed for use as a metallic degradable biomaterial for stent application, was successfully prepared by means of MIM. While the samples initially containing 62% pure iron powder in the feedstock showed a well distributed and small pore structure, the sample initially containing 66% pure iron powder exhibited a coalesced pore structure with larger pore interspaces. The amount of porosity appeared to have a major effect on the surface and mechanical properties of the sintered materials. The MIM pure iron exhibited exceptionally high ductility values (elongation to fracture varying from 13 to 50%),

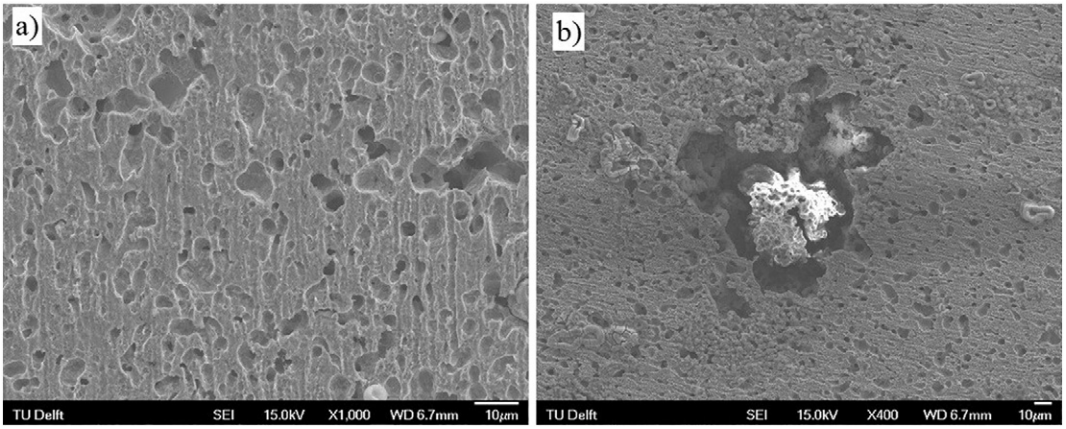

Fig. 10. Corroded 54%/1040 °C sintered sample with pitting as the main mechanism (a) an overall view and (b) a close-up view.

while the strength values fell between those of magnesium alloys and 316 L stainless steel. Interestingly, the feedstock containing 66% pure iron powder (above the critical powder loading) showed the highest elongation. Pitting corrosion occurred to the samples having experienced the lowest densification during sintering, but the main corrosion mechanism changed to uniform corrosion in the most densified samples. The in vitro corrosion rate of MIM pure iron in Hank's solution appeared to be superior to that cast pure iron. From the results obtained from this research, MIM is considered suitable for further development as a new manufacturing route for biodegradable iron stents.

Acknowledgments

The research was supported by the Coordination for the Improvement of Higher Education Personnel (CAPES) and financed by the Brazilian government under the project number CAPES/AUX 993/2009.

Appendix A. Supplementary data

Supplementary data to this article can be found online at http://dx.doi.org/10.1016/j.powtec.2016.02.042.

References

[1] C.E. Mullins, M.P. O'Laughlin, G.W. Vick, D.C. Mayer, T.J. Myers, D.L. Kearney, R.A. Schatz, J.C. Plamaz, Implantation of balloon-expandable intravascular grafts by catheterization in pulmonary arteries and systemic veins, Circulation 77 (1988) 188–199.
[2] M.P. O'Laughlin, S.B. Perry, J.E. Lock, C.E. Mullins, Use of endovascular stents in congenital heart disease, Circulation 83 (1991) 1923–1939.
[3] J.A. Suwaidi, P.B. Berger, D.R. Holmes, Coronary artery stents, J. Am. Med. Assoc. 284 (2000) 1828–1836.
[4] M. Okubo, L.N. Benson, Intravascular and intracardiac stents used in congenital heart disease, Curr. Opin. Cardiol. 16 (2001) 84–91.
[5] P.P. Mueller, T. Maya, A. Perz, H. Hauser, M. Peuster, Long-term biocompatibility of a corrodible peripheral iron stent in the porcine descending aorta, Biomaterials 27 (2006) 4955–4962.
[6] D.T. Ashby, G. Dangas, R. Mehran, M.B. Leon, Coronary artery stenting, Catheter. Cardiovasc. Interv. 56 (2002) 83–102.
[7] D.A. Puleo, W.W. Huh, Acute toxicity of metal ions in cultures of osteogenic cells derived from bone marrow stromal cells, J. Appl. Biomater. 6 (1995) 109–116.
[8] R. Waksman, Promise and challenges of bioabsorbable stents, Catheter. Cardiovasc. Interv. 70 (2007) 407–414.
[9] M. Moravej, F. Prima, M. Fiset, D. Mantovani, Electroformed iron as new biomaterial for degradable stents: development process and structure–properties relationship, Acta Biomater. 6 (2010) 1726–1735.
[10] G. Mani, M.D. Feldman, D. Patel, C.M. Agrawal, Coronary stents: a materials perspective, Biomaterials 28 (2007) 1689–1710.
[11] J. Lévesque, H. Hermawan, D. Dubé, D. Mantovani, Design of a pseudophysiological test bench specific to the development of biodegradable metallic biomaterials, Acta Biomater. 4 (2008) 284–295.
[12] R. Waksman, Update on bioabsorbable stents: from bench to clinical, J. Interv. Cardiol. 19 (2006) 414–421.
[13] X. Gu, Y. Zheng, Y. Cheng, S. Zhong, T. Xi, In vitro corrosion and biocompatibility of binary magnesium alloys, Biomaterials 9 (2009) 484–498.
[14] H. Hermawan, H. Alamdari, D. Mantovani, D. Dubé, Iron–manganese: new class of metallic degradable biomaterials prepared by powder metallurgy, Powder Metall. 51 (2008) 38–45.
[15] M. Moravej, D. Mantovani, Biodegradable metals for cardiovascular stent application: interests and new opportunities, Int. J. Mol. Sci. 12 (2011) 4250–4270.
[16] H. Hermawan, D. Mantovani, Process of prototyping coronary stents from biodegradable Fe–Mn alloys, Acta Biomater. 9 (2013) 8585–8592.
[17] B. Hausnerova, Powder injection molding — an alternative processing method for automotive items, in: M. Chiaberge (Ed.), New Trends and Developments in Automotive System Engineering, InTech, Rijeka 2011, pp. 129–146.
[18] US Patent, Metal injection molded tubing for drug eluting stents, US 8303642 B1.
[19] H. Yin, X. Qu, C. Jia, Fabrication of micro gear wheels by micropowder injection molding, J. Univ. Sci. Technol. Beijing 15 (2008) 480–484.
[20] X. Kong, T. Barriere, J.C. Gelin, Determination of critical and optimal powder loadings for 316 L fine stainless steel feedstocks for micro-powder injection molding, J. Mater. Process. Technol. 212 (2012) 2173–2182.
[21] C. Demangel, D. Auzène, M. Vayssade, J.L. Duval, P. Vigneron, M.D. Nagel, J.C. Puippe, Cytocompatibility of titanium metal injection molding with various anodic oxidation post-treatments, Mater. Sci. Eng. C 32 (2012) 1919–1925.
[22] L.J. Chen, T. Li, Y. Li, H. Hao, Y. Hu, Porous titanium implants fabricated by metal injection molding, Trans. Nonferrous Met. Soc. China 19 (2009) 1174–1179.
[23] J.P. Choi, G.Y. Lee, J.I. Song, W.S. Lee, J.S. Lee, Sintering behavior of 316 L stainless steel micro-nanopowder compact fabricated by powder injection molding, Powder Technol. 279 (2015) 196–202.
[24] N.S. Fagali, C.A. Grillo, S. Puntarulo, M.A. Fernández, L. de Mele, Cytotoxicity of corrosion products of degradable Fe-based stents: relevance of pH and insoluble products, Colloids Surf. B 128 (2015) 480–488.
[25] E. Zhang, H. Chen, F. Shen, Biocorrosion properties and blood and cell compatibility of pure iron as a biodegradable biomaterial, J. Mater. Sci. 21 (2010) 2151–2163.
[26] S. Zhu, N. Huang, L. Xu, Y. Zhang, H. Liu, H. Sun, Y. Leng, Biocompatibility of pure iron: in vitro assessment of degradation kinetics and cytotoxicity on endothelial cells, Mater. Sci. Eng. C 29 (2009) 1589–1592.
[27] American Society for Testing and Materials, ASTM-B-311: standard test methods for tension testing of metallic materials, Annual Book of ASTM Standards, 2004.
[28] F. Kafkas, T. Ebel, Metallurgical and mechanical properties of Ti–24Nb–4Zr–8Sn alloy fabricated by metal injection molding, J. Alloys Compd. 617 (2014) 359–366.
[29] G. Chen, P. Cao, N. Edmonds, Porous NiTi alloys produced by press-and-sinter from Ni/Ti and Ni/TiH2 mixtures, Mater. Sci. Eng. A 582 (2013) 117–125.
[30] American Society for Testing and Materials, ASTM-G-31: standard practice for laboratory immersion corrosion testing of metals, Annual Book of ASTM Standards, 2001.
[31] X.B. Chen, Y.C. Li, P.D. Rodgson, C. Wen, The importance of particle size in porous titanium and nonporous counterparts for surface energy and its impact on apatite formation, Acta Biomater. 5 (2009) 2290–2302.
[32] Y. Li, L. Li, K.A. Khalil, Effect of powder loading on metal injection molding stainless steels, J. Mater. Process. Technol. 183 (2007) 432–439.
[33] G. Aggarwal, I. Smid, S.J. Park, R.M. German, Development of niobium powder injection molding — part II: debinding and sintering, Int. J. Refract. Met. Hard Mater. 25 (2007) 226–236.
[34] J.P. Choi, H.G. Lyu, W.S. Lee, J.S. Lee, Densification and microstructural development during sintering of powder injection molded Fe micro-nanopowder, Powder Technol. 253 (2014) 596–601.
[35] J. Čapek, D. Vojtěch, Effect of sintering conditions on the microstructural and mechanical characteristics of porous magnesium materials prepared by powder metallurgy, Mater. Sci. Eng. C 35 (2014) 21–28.
[36] M.B. Shongwe, S. Diouf, M.O. Durowoju, P.A. Olubambi, Effect of sintering temperature on the microstructure and mechanical properties of Fe30%Ni alloys produced by spark plasma sintering, J. Alloys Compd. 649 (2015) 824–832.
[37] F. Migliavacca, L. Petrini, V. Montanari, I. Quagliana, F. Auricchio, G. Dubini, A predictive study of the mechanical behavior of coronary stents by computer modelling, Med. Eng. Phys. 27 (2005) 13–18.
[38] B. Song, S. Dong, S. Deng, H. Liao, C. Coddet, Microstructure and tensile properties of iron parts fabricated by selective laser melting, Opt. Laser Technol. 56 (2014) 451–460.
[39] D. Banerjee, J.C. Williams, Perspectives on titanium science and technology, Acta Mater. 61 (2013) 844–879.
[40] P. Bowen, J. Drelich, J. Goldman, A new in vitro–in vivo correlation for bioabsorbable magnesium stents from mechanical behavior, Mater. Sci. Eng. C 33 (2013) 5064–5070.
[41] H. Huang, C.T. Ho, T.H. Lee, T.L. Lee, K.K. Liao, F.L. Chen, Effect of surface roughness of ground titanium on initial cell adhesion, Biomol. Eng. 21 (2004) 93–97.
[42] Z. Huan, L.E. Fratila-Apachitei, I. Apachitei, J. Duszczyk, Porous NiTi surfaces for biomedical applications, Appl. Surf. Sci. 258 (2012) 5244–5249.
[43] H. Hermawan, A. Purnama, D. Dube, J. Couet, D. Mantovani, Fe–Mn alloys for metallic biodegradable stents: degradation and cell viability studies, Acta Biomater. 6 (2010) 1852–1860.
[44] G. Song, Control of biodegradation of biocompatible magnesium alloys, Corros. Sci. 49 (2007) 1696–1701.
[45] R. Waksman, R. Pakala, P.K. Kuchulakanti, R. Baffour, D. Hellinga, R. Seabron, Safety and efficacy of bioabsorbable magnesium alloy stents in porcine coronary arteries, Catheter. Cardiovasc. Interv. 68 (2006) 606–617.

P. Mariot, He graduated in Materials Engineering at University of Extremo Sul Catarinense (2005). He earned his Master's degree from Federal University of Santa Catarina (2011). Since 2013, he has been an Assistant Professor at University of Vale do Itajaí – Univali.

M.A. Leeflang, M.A. Leeflang was born in Goodwood, South Africa, in 1974. He received his B. Eng. degree in Mechanical Engineering from the University of Applied Sciences Utrecht, The Netherlands, in 2008. In 2000, he joined the Department of Materials Science and Engineering, Delft University of Technology, The Netherlands, as Laboratory Manager. Since 2011, he has been associated with the Department of Biomechanical Engineering of the same University. His current research is in the areas of powder metallurgy, additive manufacturing and (degradable) biomaterials. He has co-authored over 10 publications.

L. Schaeffer, Graduated in Mechanical Engineering from the Federal University of Rio Grande do Sul (1971). He received his PhD degree in Metal Forming from Rheinisch-Westfalischen Technischen Hochschule/Aachen (1982). Since 1976, he has been an Associate Professor at Federal University of Rio Grande do Sul. Currently he is a consultant at National Council for Scientific and Technological Development (CNPq). He is author and co-author of over two hundred publications in metal forming, powder metallurgy and biomaterials fields.

J. Zhou, Jie Zhou completed his study on materials science at Shanghai University of Technology in 1982. He earned his PhD from Delft University of Technology, the Netherlands, in 1991. Since then, he has continued to develop his expertise in powder and forming technologies for lightweight alloys and metal-matrix composites. He has (co-)authored 175 papers on solid-state processing of aluminum, magnesium and titanium alloys as well as metal-matrix composites. He is an associate professor in the Department of Biomechanical Engineering, Delft University of Technology. His current interest lies in the processing of metallic and composite biomaterials for new-generation implants and medical devices.